JOURNAL OF MATERIALS SCIENCE **35** (2000) 4055–4066

Relationship between deposition and recrystallization textures of copper and chromium electrodeposits

JOON HWAN CHOI, SOO YOUNG KANG, DONG NYUNG LEE*
School of Materials Science and Engineering, Seoul National University, Seoul 151-742, Korea

The ⟨100⟩, ⟨111⟩ and ⟨110⟩ textures of copper electrodeposits obtained from copper sulfate baths changed to the ⟨100⟩, ⟨100⟩ and ⟨$\sqrt{3}$10⟩ textures, respectively, after recrystallization. The textures of chromium electrodeposits obtained from the standard Sargent bath remained unchanged after recrystallization. The results are in agreement with the prediction of the strain energy release maximization model, in which the recrystallized grains orient themselves so that their minimum elastic modulus direction can be parallel to the absolute maximum internal stress direction due to dislocations in the non-recrystallized grains.

1. Introduction

Electrodeposits are known to have the texture. The texture varies with electrolysis conditions such as bath temperature, cathode current density, bath composition, and agitation degree of electrolytes. Finch *et al*. [1] made an extensive review of the relation between electrolysis condition and crystal growth. Pangarov [2, 3] suggested that the texture of fcc electrodeposits changed in order of ⟨111⟩, ⟨100⟩, ⟨110⟩, ⟨311⟩, and ⟨210⟩ with increasing overpotential. Lee *et al*. [4–9] have suggested a model for the evolution of textures of electrodeposits. In the model, the texture of electrodeposits changes from the orientation that places the lower energy crystal facets parallel to the substrate to the orientation that places the higher energy crystal facets parallel to the substrate, as the metallic ion concentration adjacent to the deposit increases.

The texture of electrodeposits is also related to their microstructure and surface morphology, which in turn may affect their mechanical and other properties [3, 5, 6, 9–12]. Understanding of their texture evolution is therefore very important.

Electrodeposits can undergo recrystallization when annealed. The texture of recrystallized deposits can differ from that of as-deposited state. Lee *et al*. investigated recrystallization textures of copper electrodeposits having a simple texture such as the ⟨100⟩, ⟨110⟩ or ⟨111⟩ orientation which were obtained from copper sulfate, copper fluoborate [13] and cyanide [14] baths. The ⟨100⟩, ⟨110⟩ and ⟨111⟩ orientations changed to the ⟨100⟩, ⟨$\sqrt{3}$10⟩, ⟨100⟩ orientations, respectively, after recrystallization. Similar results were obtained in silver electrodeposits [15]. The results were explained based on the strain energy release maximization model in which the recrystallized grains orient themselves so that their minimum elastic modulus directions can be parallel to the absolute maximum internal stress direction of non-recrystallized matrix (the following section).

Chromium is an interesting metal because its minimum elastic modulus directions are ⟨111⟩, whereas most bcc and fcc metals have the minimum elastic modulus directions in the ⟨100⟩ directions. Therefore, the recrystallization textures of chromium may differ from those of other cubic metals.

The objective of this study is to investigate the recrystallization textures of copper and chromium electrodeposits.

2. Strain energy release maximization model

One of the present authors [16] advanced a model for the evolution of recrystallization texture. In the model the direction of absolute maximum internal stress due to dislocations in the deformed or fabricated materials becomes parallel to the minimum Young's modulus direction in recrystallized grains, whereby the strain energy release during recrystallization can be maximized (Fig. 1). Since this concept is not well known, it is briefly explained in the following.

Supposed that the dislocation array in a crystal is depicted as shown in Fig. 2. The stress fields of the array of an infinite number of edge dislocations can be calculated by superposing the stress fields of isolated dislocations. Following Sutton and Ballufi [17], the stress fields of this array are given by

$$\sigma_{12} = -\sigma_0 \sin X_1(\cosh X_2 - \cos X_1 - X_2 \sin X_2) \quad (1)$$

* Author to whom all correspondence should be addressed.

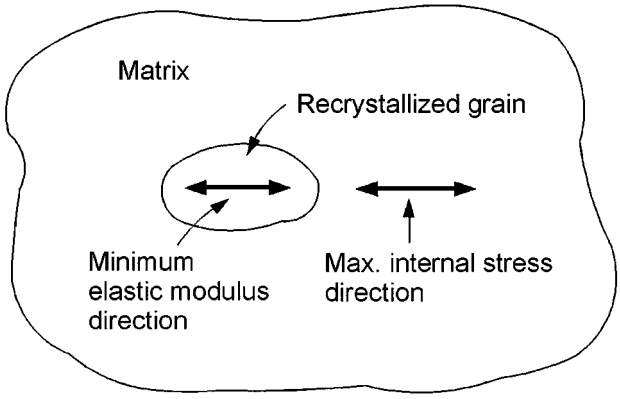

Figure 1 Matrix and recrystallized grains constitute constant volume system, in which energy release can be maximized when the absolute maximum stress direction becomes parallel to minimum elastic modulus direction of recrystallized grain.

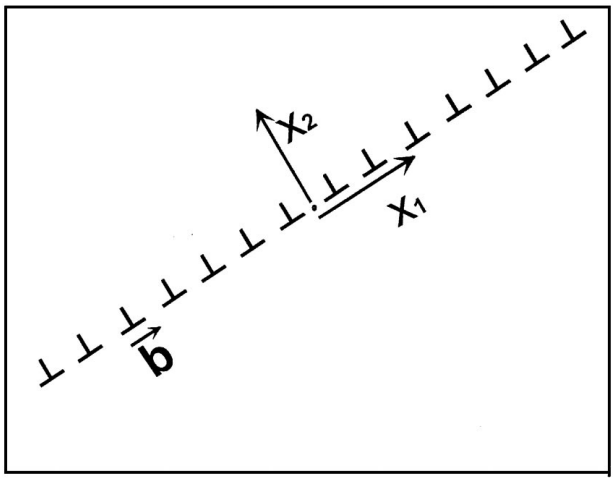

Figure 2 Coordinates in edge dislocation array.

$$\sigma_{11} = \sigma_0[2\sinh X_2(\cosh X_2 - \cos X_1) - X_2(\cosh X_2 \cos X_1 - 1)] \quad (2)$$

$$\sigma_{22} = -\sigma_0 X_2(\cosh X_2 \cos X_1 - 1) \quad (3)$$

where $X_1 = 2\pi x_1/D$, $X_2 = 2\pi x_2/D$ and $\sigma_0 = -Gb/[2D(1-v)(\cosh X_2 - \cos X_1)^2]$ with G, b, v, and D being the shear modulus, the Burgers vector, Poisson's ratio, and the distance between dislocations, respectively.

As $x_2 \to \pm\infty$, it is seen that σ_{22} and σ_{12} tend to zero exponentially, but

$$\sigma_{11} \to \frac{Gb}{D(1-v)}\mathrm{sgn}(x_2) \quad (4)$$

where $\mathrm{sgn}(x_2) = -1$ if $x_2 > 0$ and $\mathrm{sgn}(x_2) = 1$ if $x_2 < 0$.

The absolute maximum stress, $|\sigma_{\max}| = |(\sigma_{11} + \sigma_{22})/2 + [(\sigma_{11} - \sigma_{22})^2/4 + \sigma_{12}^2]^{1/2}|$, approaches $|\sigma_{11}|$ exponentially as $|x_2|$ increases above $D/2\pi$. Therefore, the maximum stress direction is parallel to the Burgers vector direction. Fig. 3 shows a few examples of the calculated principal stress distribution in the array of parallel edge dislocations, which show that the maximum stress direction is along the Burgers vector direction. It is noted that the stress is an internal stress.

For electrodeposits, the absolute maximum internal stress direction can be determined by the texture of deposits. The density of dislocations whose Burgers vectors are directed away from the growth direction of deposits was supposed to be higher than when the Burgers vector is nearly parallel to the growth direction, because dislocations whose Burgers vector is close to the growth direction are easy to glide out from the deposit by the image force during its growth [18]. Therefore, the absolute maximum internal stress direction is along the Burgers vector which is close to the direction normal to the growth direction.

Now that the absolute maximum internal stress of the deposit is known, we are in position to determine the orientation of recrystallized grains referred to the orientation of matrix. If a small volume in an uniaxially stressed body whose ends are fixed is replaced by the same volume of stress free body, the strain energy of the system including the replaced region will be reduced. The released strain energy is represented as the area OAB in Fig. 4. The released energy will be changed by Young's modulus of the substituted body. The released energy will be maximized, when Young's modulus of the substituted body is minimum.

From the facts that recrystallization is a displacement controlled process because the volume and shape of material do not change during recrystallization and the absolute maximum internal stress due to the dislocation array is approximated by the uniaxial stress, the matrix and the recrystallized grain can be approximately equivalent to the stressed body and the substituted body in Fig. 4, respectively.

Therefore, we can address that the strain energy release can be maximized when the direction of absolute maximum internal stress due to dislocations in the matrix becomes parallel to the minimum Young's modulus direction in recrystallized grains. In the real situation, the stress field is triaxial. However, this simple concept can be a starting point.

This model could explain the evolution of recrystallization textures from deformation textures, even though the method of determining the absolute maximum internal stress direction is different from that in the case of electrodeposits [18–26]. It should be emphasized that the model cannot apply to materials, in which dislocations cannot be a dominant driving force for recrystallization [27].

3. Experimental

About 35 μm thick copper electrodeposits were obtained from copper sulfate baths. Electrodeposition conditions are given in Table I. A 316L stainless steel sheet was used as cathode and a lead sheet was used as insoluble anode. The deposits were peeled off from the cathode. The peeled deposits were annealed in a potassium nitrate salt bath.

Chromium was electrodeposited from a Sargent bath containing 2.5 M CrO_3, 0.0255 M H_2SO_4. In order to prevent gas evolution, 0.2 g/l Zero mist (HT-2) was

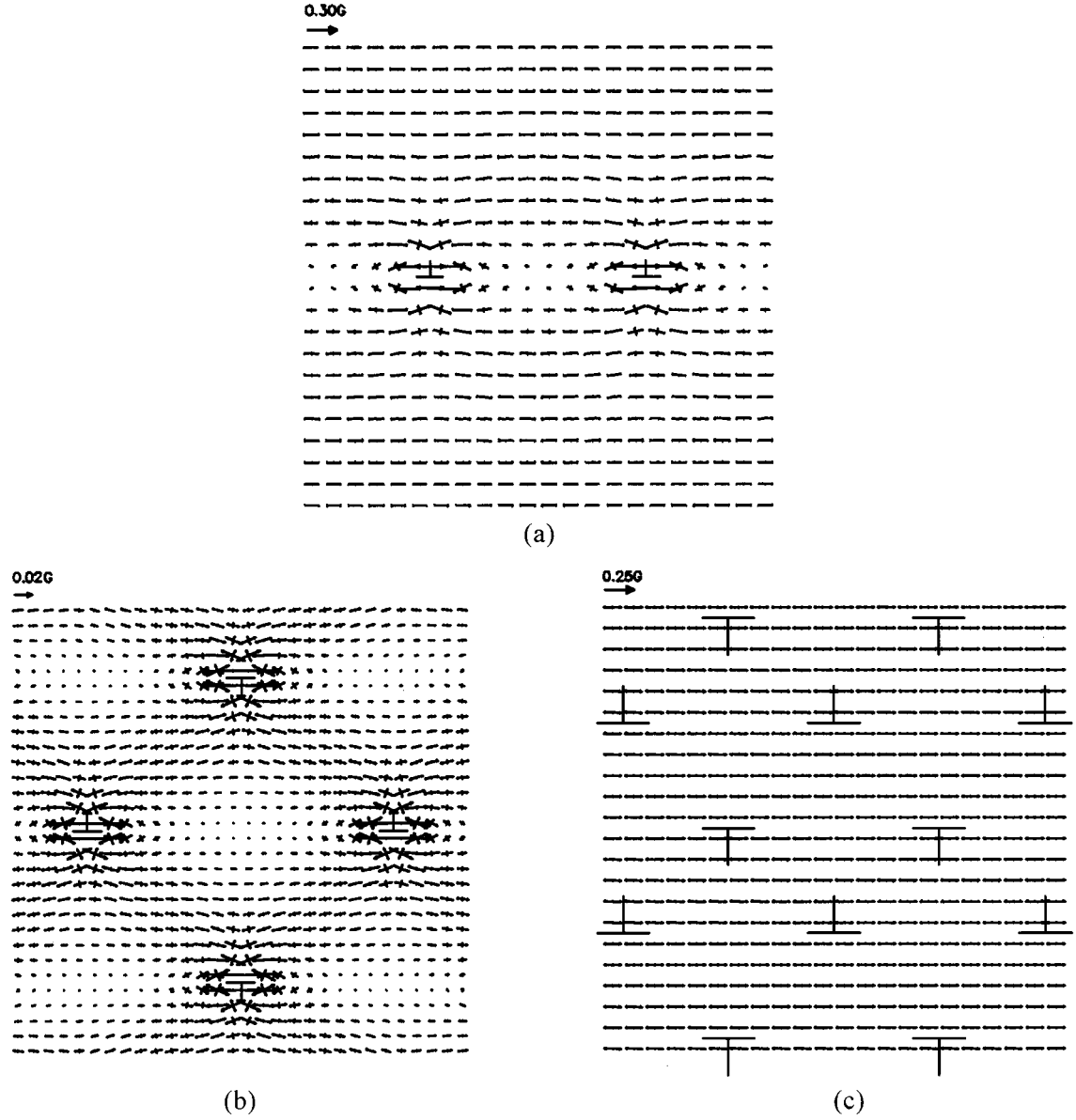

Figure 3 Principal stress distributions around parallel edge dislocations based on (a) 100 linearly arrayed dislocations with dislocation spacing is 10b, (b) low energy array of 20 × 20 dislocations with horizontal dislocation spacing of 20b, and (c) low energy array of 100 × 100 dislocations with horizontal dislocation spacing of 10b. *b* is Burgers vector and *G* is shear modulus.

TABLE I Copper electrodeposition condition

Bath	Bath Composition	Temp. (K)	Cathode C.D ($A \cdot m^{-2}$)	Specimen	Annealing
A	1.00M $CuSO_4 \cdot 5H_2O$ 0.714M H_2SO_4	303	50	Cu(100)	773K, 5 h
B	1.12M $CuSO_4 \cdot 5H_2O$ 0.816M H_2SO_4	303	600 800	Cu(110) Cu(111)	673K, 10 m 873K, 1 h

TABLE II Chromium electrodeposition conditions

Condition	Bath Temp. (K)	Cathode Current Density ($A \cdot m^{-2}$)	Stirring	Specimen
cond-A	338	2500	Stirred	Cr(111)
cond-B	313	2500	Stirred	$Cr(111)_a$
cond-C	293	5000	Not stirred	$Cr(100)_a$

added to the bath. A copper sheet of 0.1 mm in thickness and 48 × 76 mm^2 in area was used as cathode after polishing, followed by degreasing and acid dipping. A lead sheet of 1.8 mm in thickness and 48 × 76 mm^2 in area was used as insoluble anode. The inter-electrode distance was 50 mm.

Chromium electrodeposits obtained under various electrolysis conditions are summarized in Table II. The copper substrate was dissolved in 30%HNO_3 for 10 min. to obtain the chromium deposit only. The chromium deposit was annealed at various temperatures for 1 hour and at 903 K for various times in vacuum chamber of 10^{-5} torr. The hardness was measured with a Knoop hardness tester under a load of 50 g.

The textures of the deposits were measured using a diffractometer or a pole figure goniometer. The measurement of pole figures was carried out by the Schultz reflection method with Zr filtered Mo K_α radiation. In the case using the diffractometer, the orientation of the deposit was expressed in terms of texture factors of reflection planes.

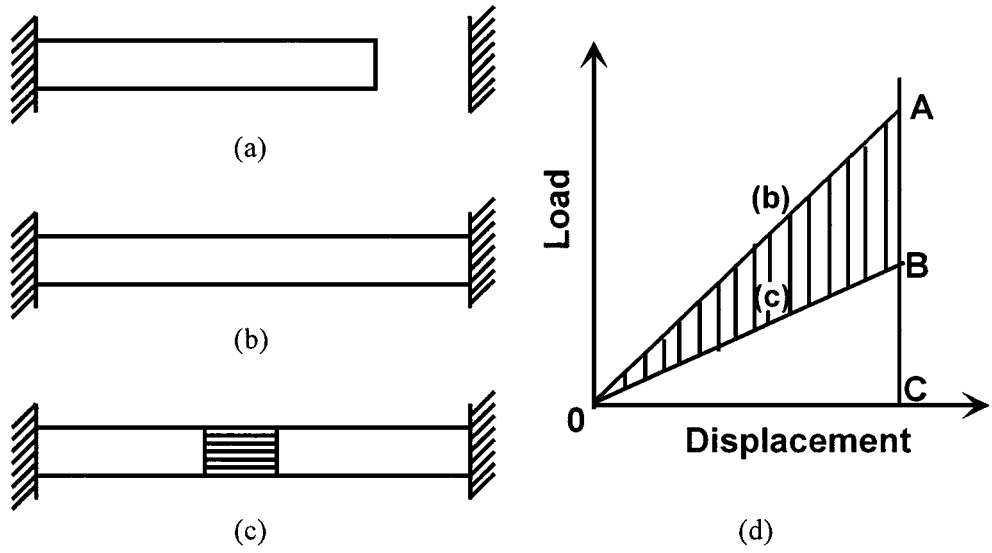

Figure 4 A stress free body (a) is elongated and its both ends are fixed (b). The strain energy of the body is represented by the area OAC. When small portion of the stressed body is replaced by a stress free material, The strain energy of system is reduced to the area OBC and the energy release is represented by the area OAB.

The texture fraction, TF, of the (hkl) plane is defined by

$$\mathrm{TF(hkl)} = \frac{I(\mathrm{hkl})/I_0(\mathrm{hkl})}{\sum[I(\mathrm{hkl})/I_0(\mathrm{hkl})]} \qquad (5)$$

where I(hkl) and I_0 (hkl) are the integrated intensities of (hkl) reflections measured for experimental specimen and a standard powder sample, respectively, and Σ means the summation. The summation of TFs of all the reflection planes is equal to unity. When the TF of any (hkl) plane is larger than the mean value of TFs, a preferred orientation or a texture exists in which grains are oriented with their (hkl) planes parallel to the surface. When the TFs of all reflection planes are the same, the deposit has the random orientation.

The more accurate orientation can be obtained from pole figures. In order to measure the growth orientation of copper electrodeposits, the {111}, {200} and {220} pole figures were measured using the Schultz pole figure device. The pole figure data were used to calculate the inverse pole figures [28].

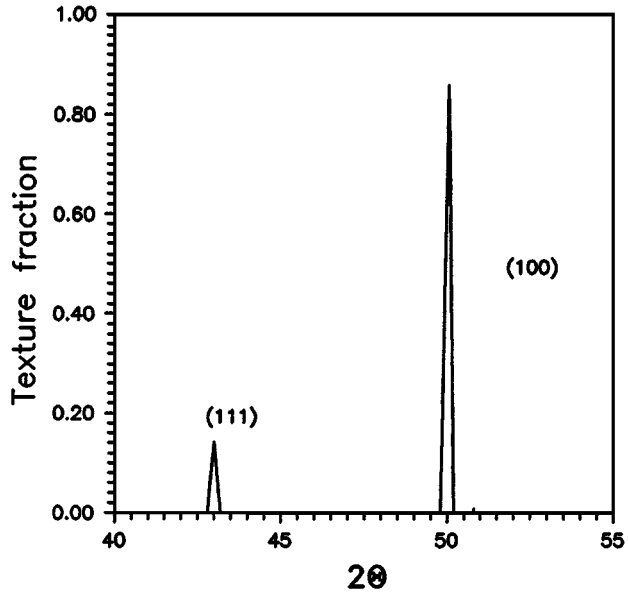

Figure 5 Texture fractions of (111) and (100) planes of Specimen Cu(100) before and after annealing at 773 K for 5 h. Peaks from annealed specimen were almost the same as those from as-deposited one.

4. Results

The texture fractions of the {111} and {100} planes of Specimen Cu(100) remained unchanged even after annealing at 773 K for up to 5 h. The texture fractions are shown in Fig. 5. The other reflection peaks did not appear in Specimen Cu(100). This indicates that Specimen Cu(100) had the ⟨100⟩ growth orientation, which remained unchanged even after annealing. Fig. 6 shows the inverse pole figures of Specimen Cu(111) before and after annealing at 873 K for 1 h, which indicates that Specimen Cu(111) had the ⟨111⟩ growth orientation, which changed to ⟨100⟩ after annealing. Fig. 7 shows the inverse pole figures of Specimen Cu(110) before and after annealing at 673 K for 10 min. This specimen had the ⟨110⟩ orientation, which changed to the $\langle\sqrt{3}10\rangle$ orientation after annealing.

These results are the same as the previous results, in which the ⟨100⟩, ⟨111⟩ and ⟨110⟩ deposition textures changed the ⟨100⟩, ⟨100⟩ and $\langle\sqrt{3}10\rangle$ recrystallization textures [13].

Table III shows the texture fractions of chromium electrodeposits obtained under three electrodeposition conditions. Specimen Cr(111) has a very strong ⟨111⟩ fiber texture. The texture of Specimen $\mathrm{Cr(111)_a}$ can be approximated by the ⟨111⟩ orientation, whose orientation intensity was weaker than that of Specimen Cr(111). The texture of Specimen $\mathrm{Cr(100)_a}$ may be approximated by the ⟨100⟩ fibre texture.

Figs 8 and 9 show the optical microstructures and the hardnesses of Specimen Cr(111) when annealed at various temperatures for 1 hour, respectively. The microstructure of the deposit remained unchanged up to 823 K. Partial recrystallization of the electrodeposit

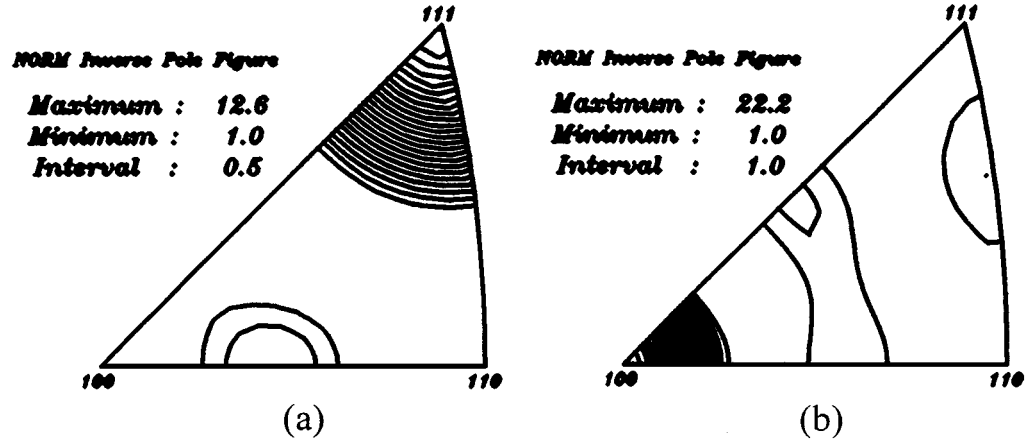

Figure 6 Inverse pole figures of Specimen Cu(111) (a) before and (b) after annealing at 873 K for 1 h.

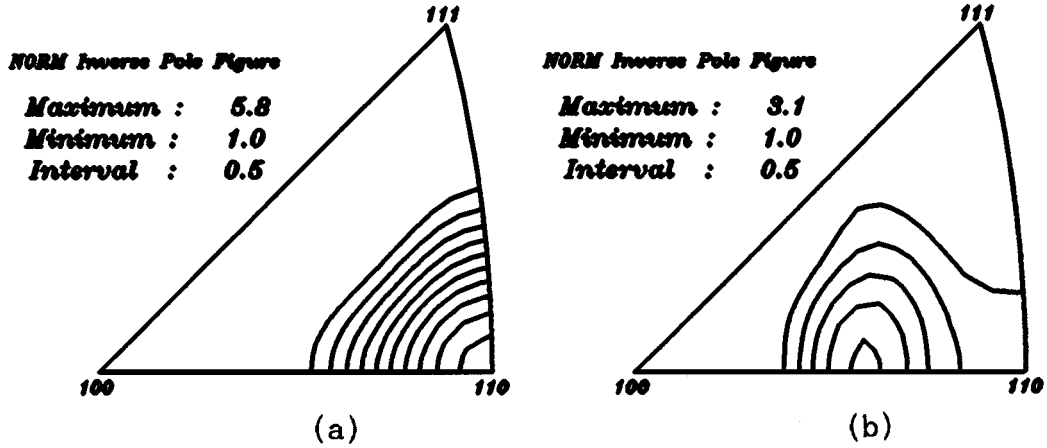

Figure 7 Inverse pole figures of Specimen Cu(110) (a) before and (b) after annealing at 673 K for 10 min.

TABLE III Texture fractions of re ection planes of chromium electrodeposits

Specimen \ Plane	(110)	(200)	(211)	(220)	(310)	(222)	Texture
Cr(111)	0.02	0.05	0	0	0	**0.93**	Very strong ⟨111⟩ bre texture
$Cr(111)_a$	0.03	0.15	0.28	0	0.01	**0.53**	⟨111⟩
$Cr(100)_a$	0.19	**0.47**	0.13	0.05	0.13	0.03	⟨100⟩

took place at 903 K, and complete recrystallization was observed at temperatures above 973 K. Fig. 10 shows the texture fractions of Specimen Cr(111) when annealed at various temperatures for 1 hour. Fig. 11 shows the texture fractions of Specimen Cr(111) annealed at 903 K for various periods of time. It can be seen that the ⟨111⟩ texture of chromium electrodeposit did not change even after recrystallization.

Fig. 12 shows the texture fractions of Specimen $Cr(111)_a$ annealed at various temperatures for 1 h. Fig. 13 shows the texture fractions of Specimen $Cr(111)_a$ annealed at 903 K for various periods of time. The optical microstructures of Specimen $Cr(111)_a$ before and after annealing at 1173 K for 1 h is shown in Fig. 14. It can be seen that the annealed Specimen $Cr(111)_a$ was fully recrystallized and the texture fractions changed slightly. Fig. 15 shows the measured (200) pole figures of Specimen $Cr(111)_a$ before and after annealing at 1173 K for 1 h, which indicate no texture change took place after recrystallization.

Fig. 16 shows the optical microstructures of Specimen $Cr(100)_a$ before and after annealing at 1173 K for 1 hour, which indicate that the annealed specimen was fully recrystallized. The measured (200) pole figures of Specimen $Cr(100)_a$ before and after annealing at 1173 K for 1 hour are shown in Fig. 17. The chromium electrodeposit having major ⟨100⟩ orientation did not undergo the texture change even after recrystallization.

5. Discussion

The minimum elastic modulus directions of copper and chromium crystals are calculated. The elastic modulus

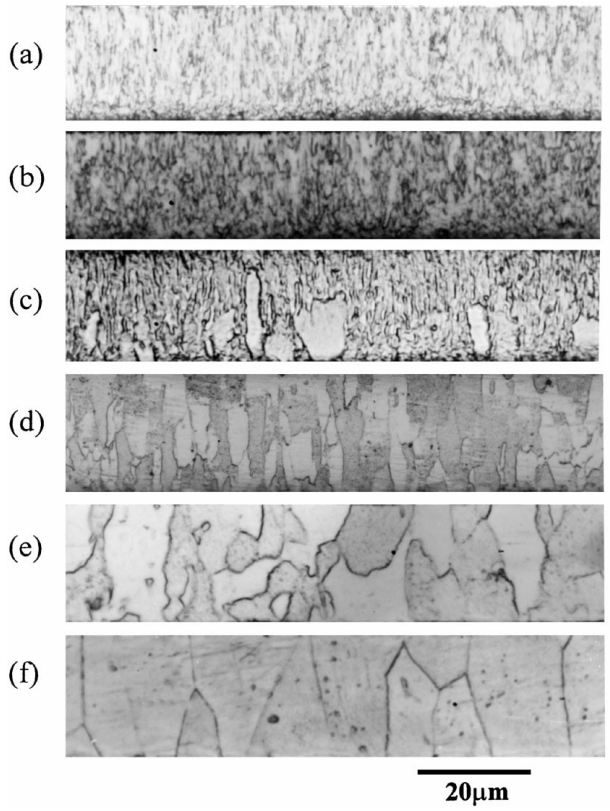

Figure 8 Optical microstuctures of Specimen Cr(111) after annealing for 1 hour at (a) room temperature, (b) 823 K, (c) 903 K, (d) 973 K, (e) 1173 K and (f) 1289 K.

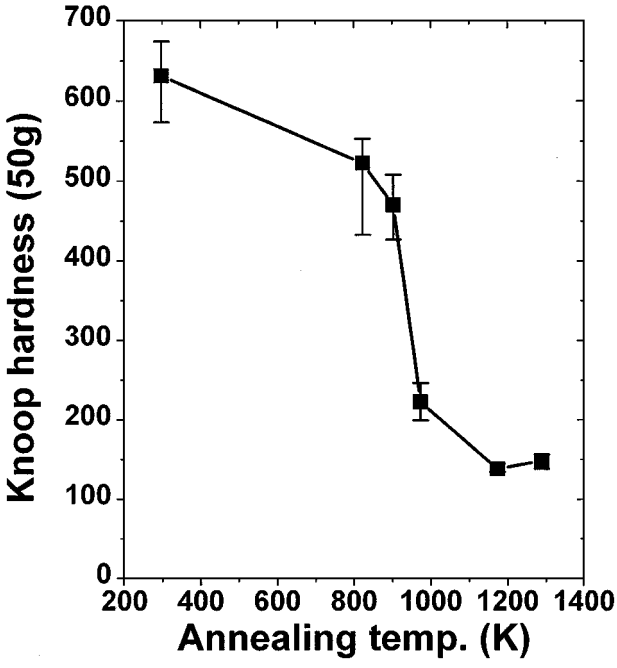

Figure 9 Hardness of Specimen Cr(111) as function of annealing temperature for 1 hour.

E of crystals can be calculated using the following relation.

$$E = \frac{1}{S'_{1111}} \tag{6}$$

where S'_{1111} is a component of compliance tensor, and is, for a material with cubic symmetry, given by [e.g. ref. 29]

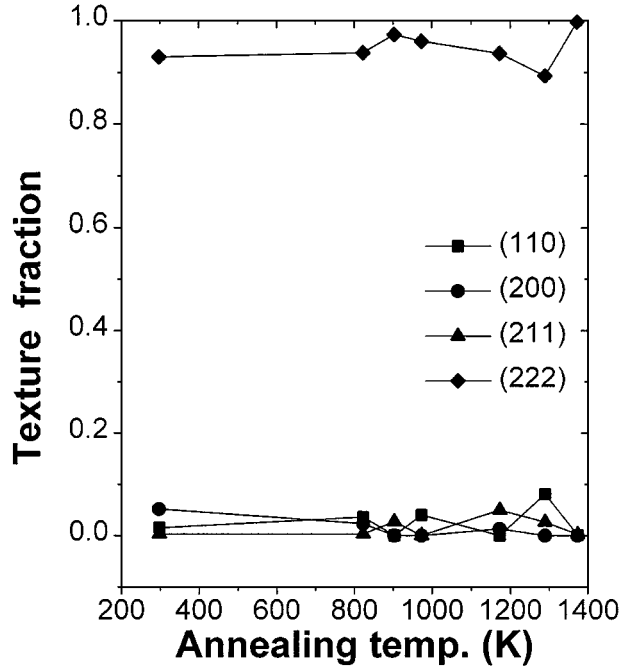

Figure 10 Texture fraction of Specimen Cr(111) as function of annealing temperature for 1 hour.

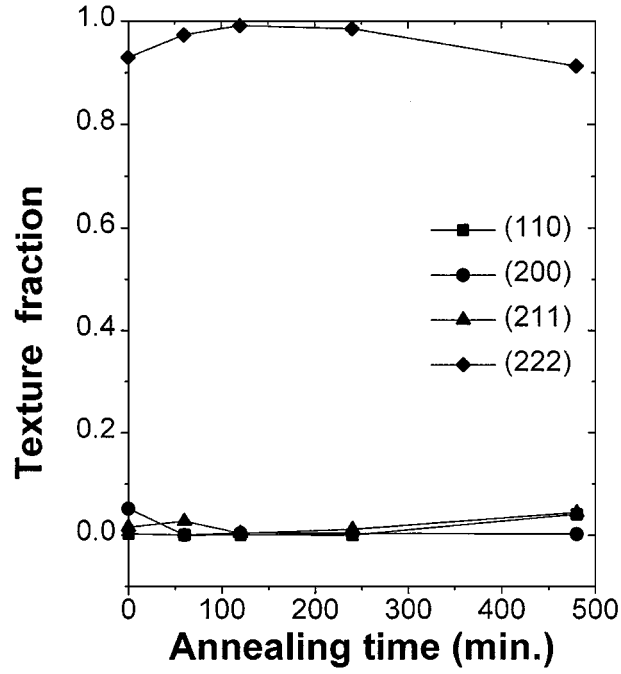

Figure 11 Texture fraction of Specimen Cr(111) as function of annealing time at 903 K.

$$S'_{1111} = S_{11} + [S_{44} - 2(S_{11} - S_{12})] \times \left(a_{11}^2 a_{12}^2 + a_{12}^2 a_{13}^2 + a_{13}^2 a_{11}^2\right) \tag{7}$$

where the direction cosines, a_{1i}, relate the arbitrary direction x'_1 to the symmetry axes, x_i.

The elastic moduli of copper at 298 K and chromium at 298 K and 500 K, which are calculated using data given in Table IV, are shown in Fig. 18 as a function of crystallographic direction. It can be seen that copper has the minimum Young's modulus along the ⟨100⟩ directions, whereas chromium has the minimum Young's modulus along the ⟨111⟩ directions.

TABLE IV Stiffness C_{ij} and compliance S_{ij} of copper and chromium [30, 31]

Crystal	Temp. (K)	C_{11}, GPa	C_{44}, GPa	C_{12}, GPa	S_{11}, GPa^{-1}	S_{44}, GPa^{-1}	S_{12}, GPa^{-1}
Cu	298	168.4	75.4	121.4	0.01498	0.01326	−0.00629
Cr	298	350	100.8	67.8	0.00305	0.009921	−0.000495
Cr	500	346	98.7	76.2	0.00314	0.0101	−0.000567

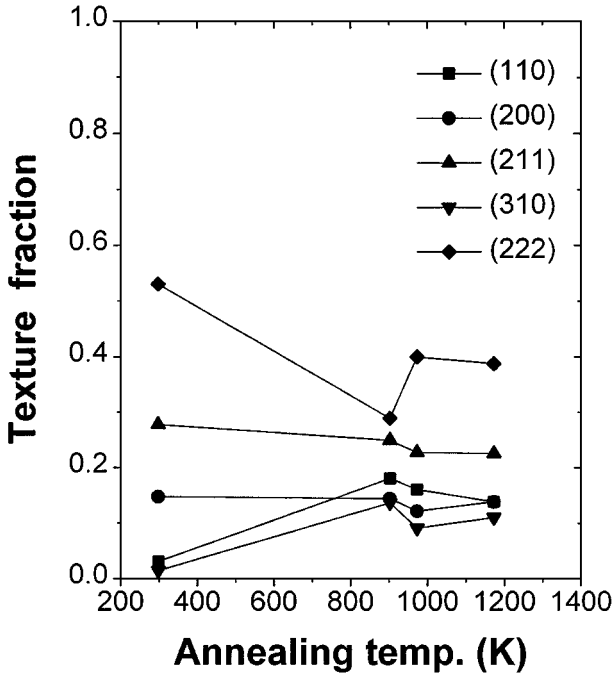

Figure 12 Texture fractions of Specimen Cr(111)a as function of annealing temperature for 1 hour.

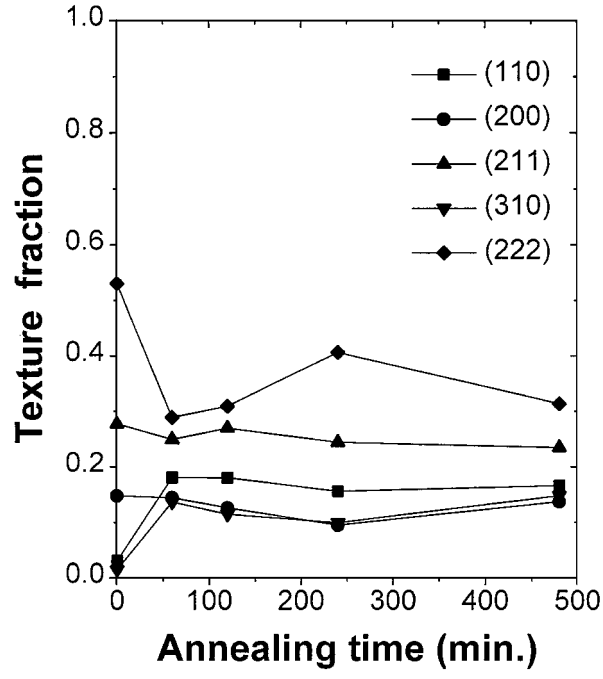

Figure 13 Texture fraction of Specimen Cr(111)a as function of annealing time at 903 K.

Once the absolute maximum internal stress directions and the minimum Young's modulus directions are known, we are in position to discuss the recrystallization textures of electrodeposits based on the strain energy release maximization model. However, in order

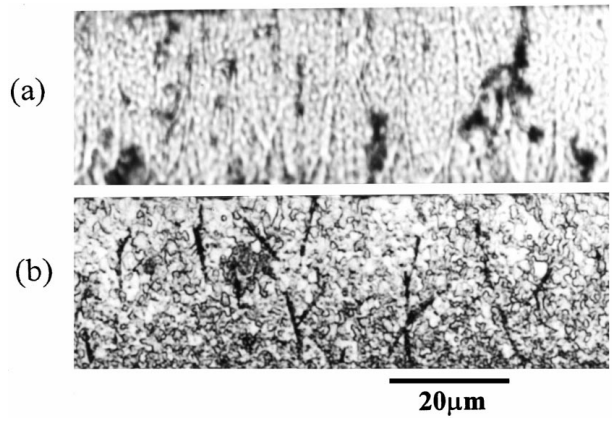

Figure 14 Optical microstuctures of Specimen Cr(111)a (a) before and (b) after annealing at 1173 K for 1 hour.

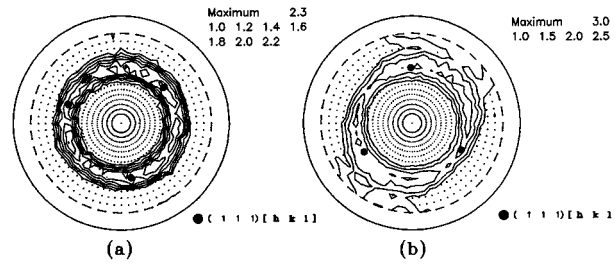

Figure 15 Measured (200) pole figures of Specimen Cr(111)a (a) before and (b) after annealing at 1173 K for 1 hour.

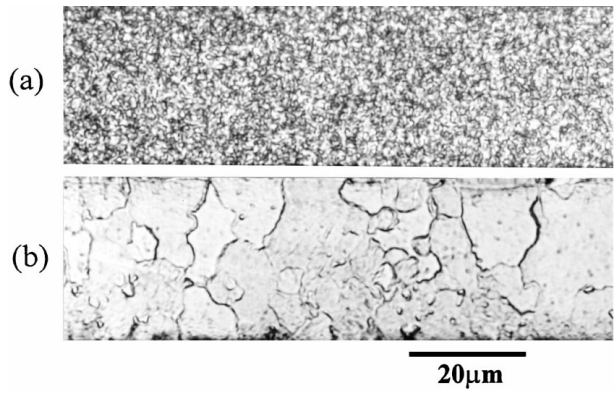

Figure 16 Optical microstuctures of Specimen Cr(100)a (a) before and (b) after annealing at 1173 K for 1 hour.

for the model to be used, the deposits must have a high dislocation density. Fig. 19 shows a TEM micrograph of Specimen Cu(111). Fig. 20 shows a TEM micrograph of Specimen Cr(111). The both specimens show high dislocation densities.

5.1. Copper electrodeposits

The minimum elastic modulus directions and the Burgers vectors of copper are along the ⟨100⟩ directions

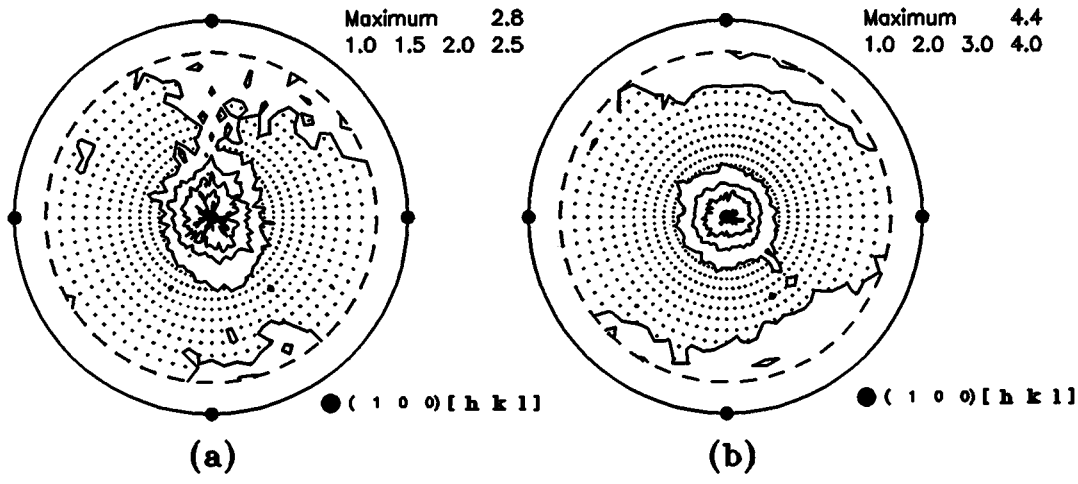

Figure 17 Measured (200) pole figures of Specimen Cr(100)a (a) before and (b) after annealing at 1173 K for 1 hour.

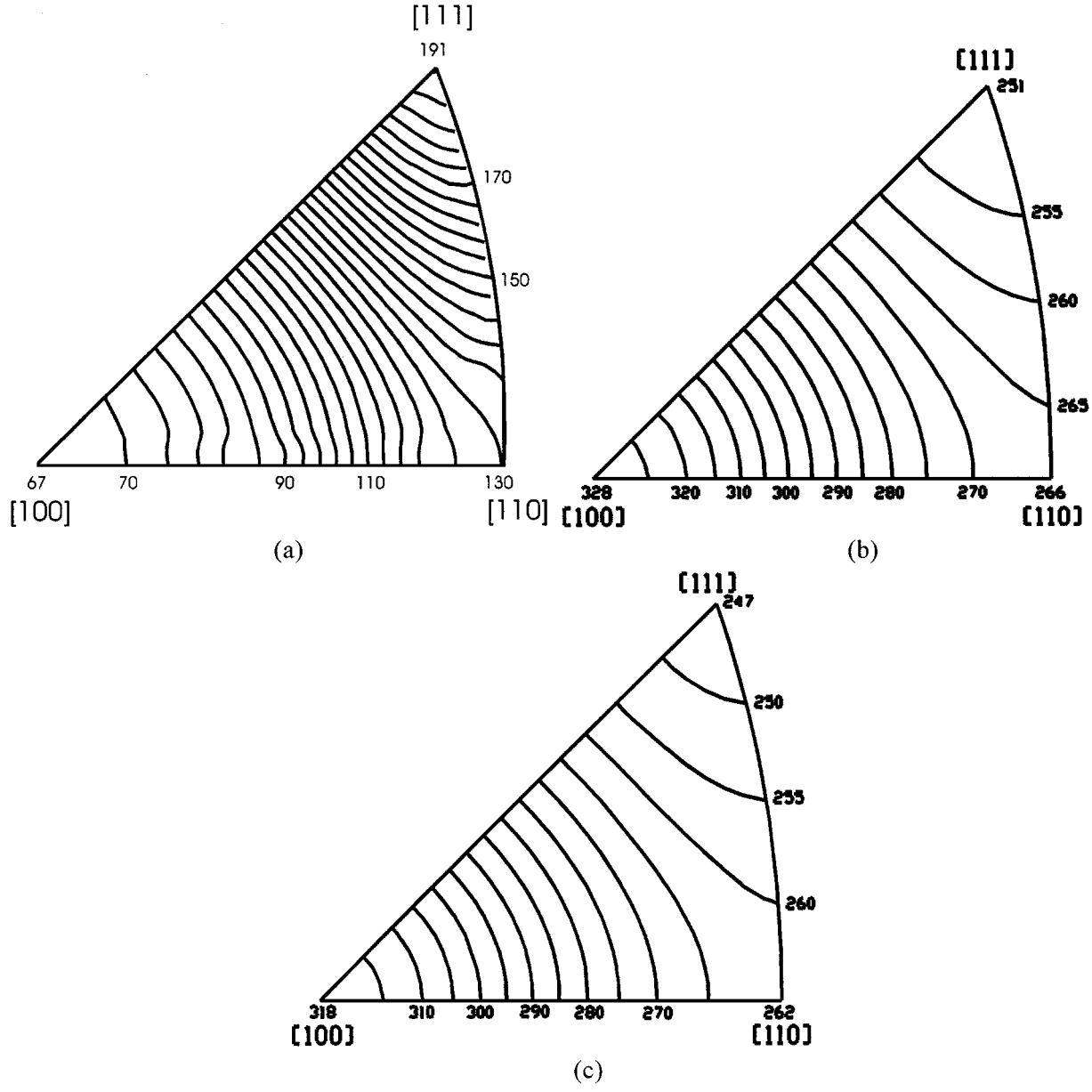

Figure 18 Young's moduli along various directions of (a) copper at 298 K and chromium crystals at (b) 298 K and (c) 500 K. (unit : GPa)

and the ⟨110⟩ directions, respectively. There are six equivalent directions in the ⟨110⟩ directions, with opposite directions being taken as the same. As already explained in the model section, the absolute maximum internal stress direction is along the Burgers vector which is approximately normal to the growth direction. Therefore, for copper deposits, the ⟨110⟩ directions at right angles or near right angles to the thickness

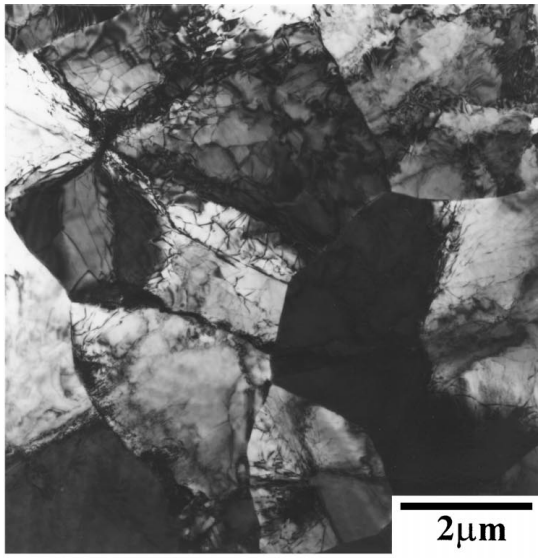

(a)

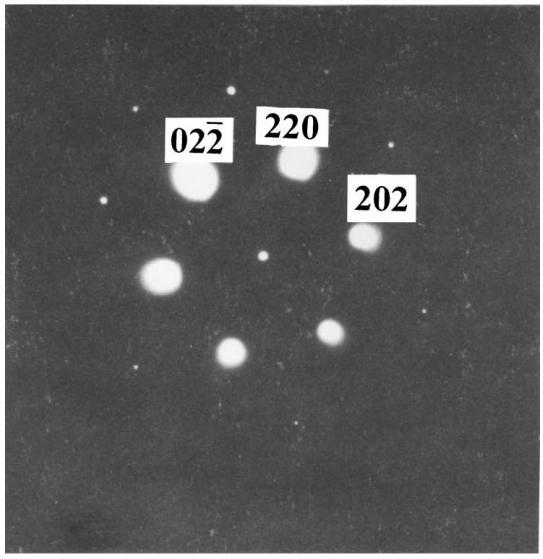

(b)

(c)

Figure 19 TEM microstructures of Specimen Cu(111) before annealing: (a) bright field image, (b) selected area diffraction pattern for a grain showing spot pattern with ⟨111⟩ zone axis and (c) bright field image showing dislocation arrays in a grain.

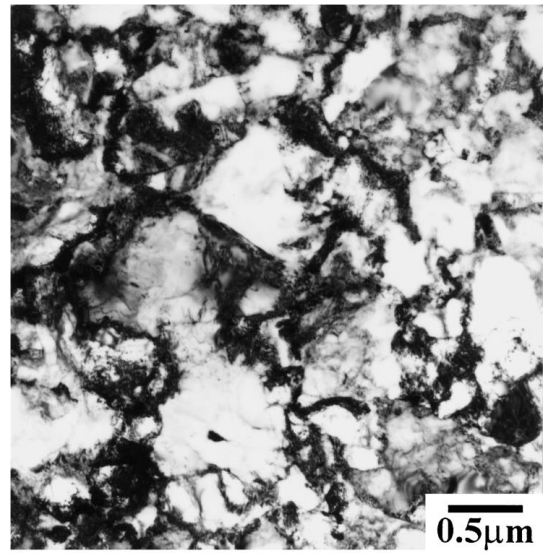

(a)

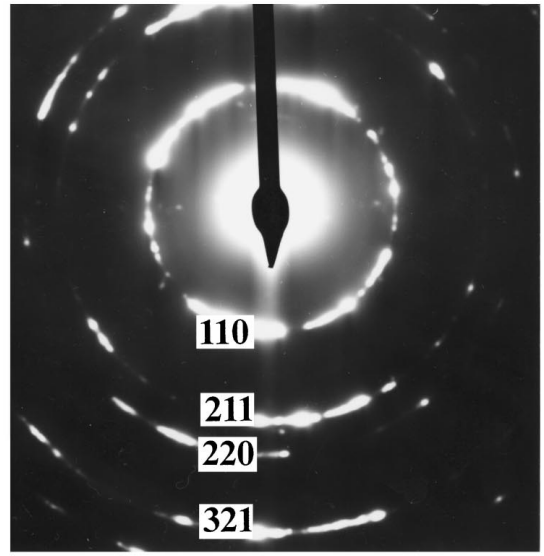

(b)

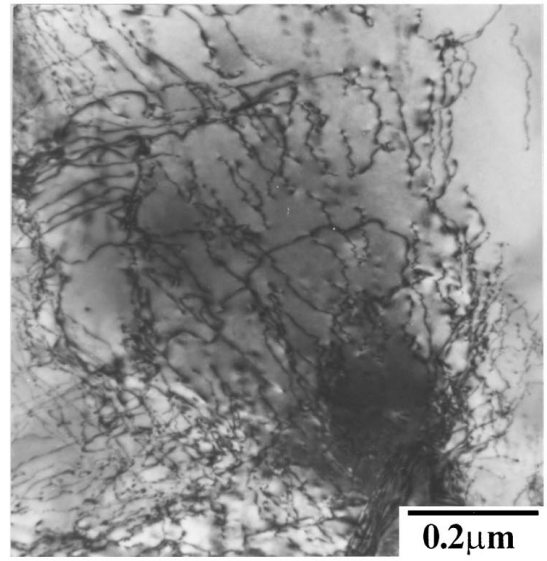

(c)

Figure 20 TEM microstructures of Specimen Cr(111) before annealing: (a) bright field image, (b) selected area diffraction pattern showing ring pattern with ⟨111⟩ zone axis and (c) bright field image showing dislocation arrays in a grain.

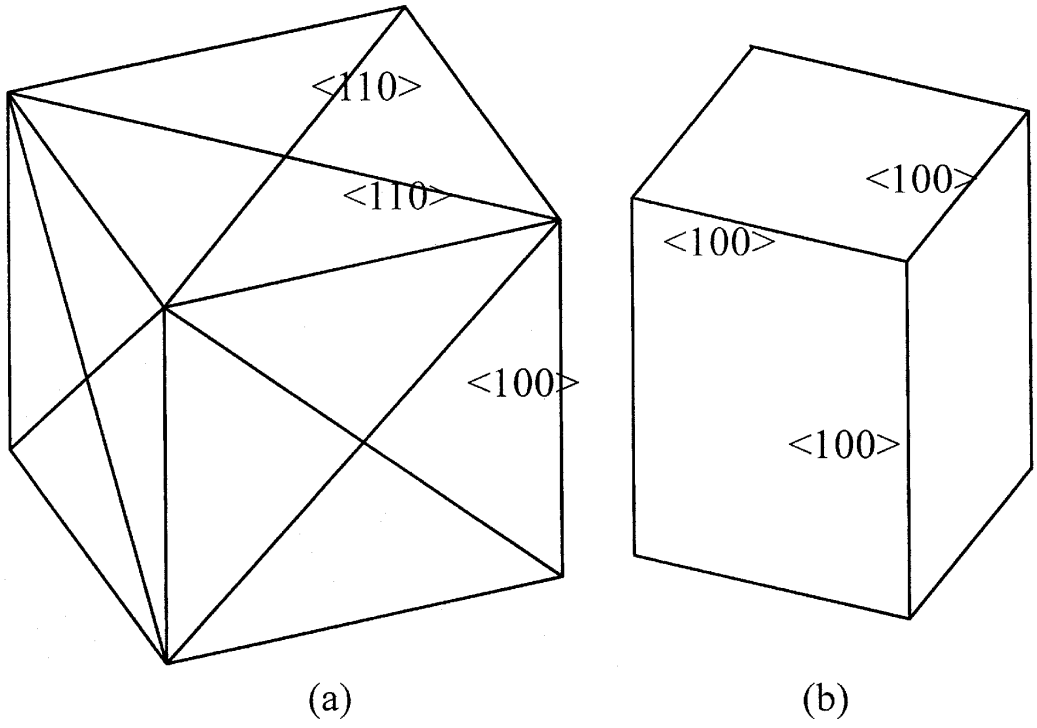

Figure 21 Drawings explaining that the ⟨100⟩ texture of copper deposit remains unchanged after recrystallization: (a) before and (b) after recrystallization.

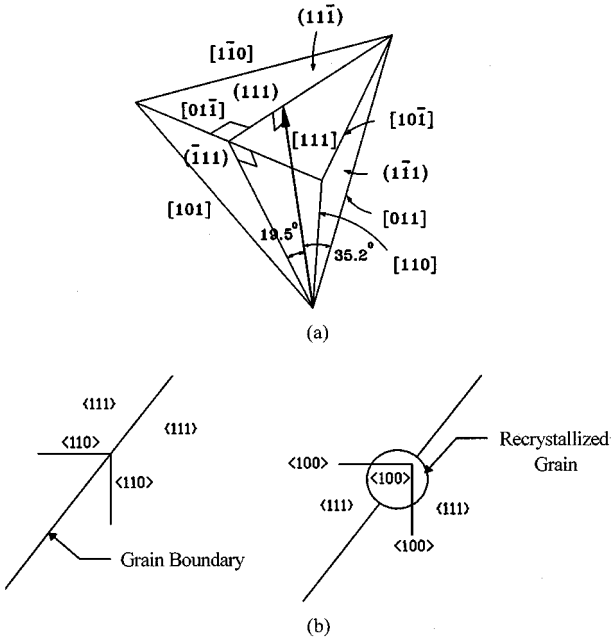

Figure 22 Drawings (a) showing ⟨110⟩ directions in ⟨111⟩ textured material in which arrow indicates direction of growth and (b) explaining that ⟨111⟩ deposition texture changes to ⟨100⟩ recrystallization texture.

direction of the deposit become the ⟨100⟩ directions after recrystallization.

For the copper deposit with the ⟨100⟩ texture, two of the six ⟨110⟩ directions are at right angles; the remaining four are at an angle of 45° to the thickness direction, as shown in Fig. 21a. The two ⟨110⟩ directions normal to the thickness direction will change to the ⟨100⟩ directions after recrystallization. The recrystallized deposit would then have the ⟨100⟩ texture, as shown in Fig. 21b, in agreement with the experimental result.

For the copper deposit with the ⟨111⟩ texture, three of the six ⟨110⟩ directions are at right angles to the thickness direction; the remaining three ⟨110⟩ directions are at an angle of 35.26° to the thickness direction, as shown in Fig. 22a. The former three ⟨110⟩ directions will be able to change to the ⟨100⟩ directions, after recrystallization, but angles between the ⟨110⟩ directions are 60° and the angle between the ⟨100⟩ directions is 90°. Correspondence between the ⟨110⟩ directions in as-deposited grain and the ⟨100⟩ directions in recrystallized grains is therefore impossible in a grain. Two of the ⟨110⟩ directions in neighboring grains, that are at right angles, can change to the ⟨100⟩ directions to form nuclei having the ⟨100⟩ texture in grain boundaries, which grow at the expense of a high dislocation region, as shown in Fig. 22b. Thus, the ⟨111⟩ deposition texture will change into the ⟨100⟩ recrystallization texture, in agreement with the experimental result.

For the ⟨110⟩ texture, one ⟨110⟩ direction is normal to the ⟨110⟩ thickness direction; the remaining four ⟨110⟩ directions are at angle of 60° to the ⟨110⟩ thickness direction, as shown in Fig. 23. The first one of the ⟨110⟩ directions and the last four ⟨110⟩ directions are likely to determine the recrystallization texture because the last four directions are closer to the planar direction than to the thickness direction. Recalling that the ⟨110⟩ directions change to ⟨100⟩ directions after recrystallization, the thickness direction of recrystallized grains should be at angles of 60 and 90° with the ⟨100⟩ directions at the same time. The thickness direction satisfying the condition is $\langle\sqrt{3}10\rangle$, in agreement with the experimental results.

In summary the ⟨100⟩, ⟨111⟩, and ⟨110⟩ deposition textures change into the ⟨100⟩, ⟨100⟩, and $\langle\sqrt{3}10\rangle$ recrystallization textures, respectively.

5.2. Chromium electrodeposits

There are four equivalent ⟨111⟩ directions in bcc chromium crystal, with opposite directions being taken

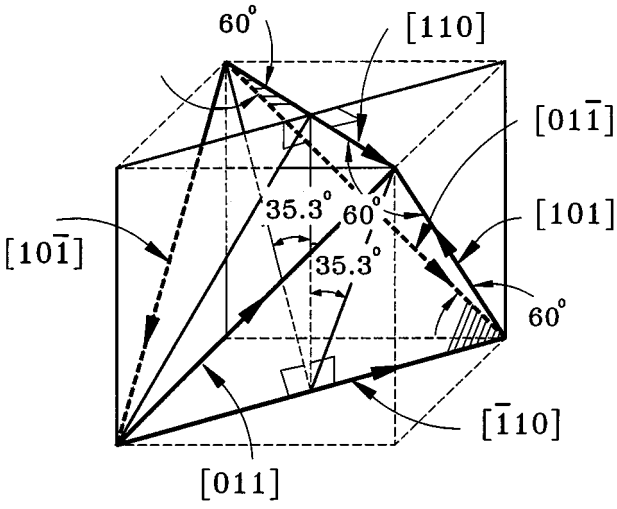

Figure 23 ⟨110⟩ directions in ⟨110⟩ oriented crystal.

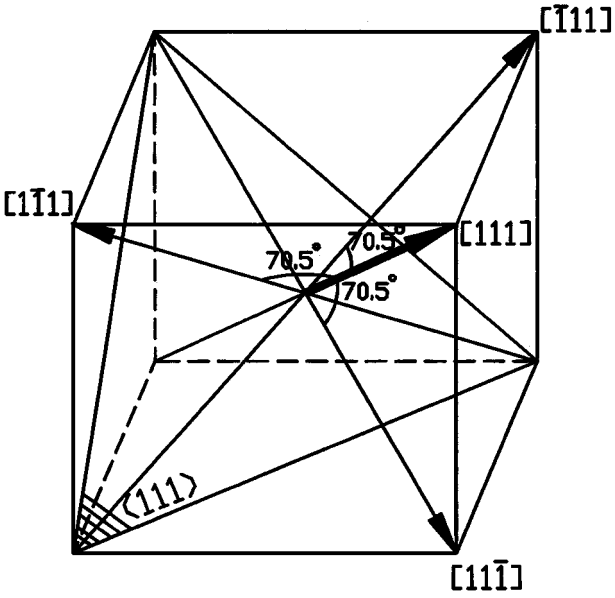

Figure 24 ⟨111⟩ directions in ⟨111⟩ textured material. Thick arrow indicates growth directions of electrodeposit.

as the same. In case of the ⟨111⟩ fiber texture of chromium, one of four ⟨111⟩ directions is parallel to the thickness direction and the remaining three ⟨111⟩ directions are at an angle of 70.5° to the thickness direction of electrodeposit as shown in Fig. 24. The remaining three ⟨111⟩ directions can be the absolute maximum internal stress directions. They will become parallel to the minimum Young's modulus directions of recrystallized grains, according to the strain energy release maximization model. The minimum Young's modulus directions of chromium are also the ⟨111⟩ directions. Therefore, the ⟨111⟩ texture of chromium will not change after recrystallization. However, Specimen $Cr(111)_a$, which has a less well developed ⟨111⟩ orientation, showed a little different evolution behavior of recystallization texture. Similarly, the ⟨100⟩ texture of chromium deposits can easily be shown to remain unchanged after recrystallization. Other texture components are likely to remain unchanged after recrystallization.

The deposition texture of Specimen Cr(111), which has the well developed ⟨111⟩ orientation, did not change after recrystallization in agreement with the prediction of the model (Figs 10 and 11). However, Specimen $Cr(111)_a$, which has a less well developed ⟨111⟩ orientation, showed a little different texture evolution behavior (Figs 12 and 13). Even though each texture component remains unchanged after recrystallization, its recrystallization rate can be different each other. If the ⟨110⟩ grains recrystallized earlier than the ⟨111⟩ grains when the specimen was annealed at 903 K, the texture change shown in Figs 12 and 13 could take place. Fig. 17 shows that Specimen $Cr(100)_a$ did not undergo a change in texture when annealed as expected.

Thus, the experimental texture results can be very well explained using the strain energy release maximization model.

6. Conclusion

The ⟨100⟩, ⟨111⟩ and ⟨110⟩ deposition texture of copper electrodeposits changed to the ⟨100⟩, ⟨100⟩ and $\langle\sqrt{3}10\rangle$ recrystallization textures, respectively, when annealed.

The ⟨111⟩ and ⟨100⟩ deposition textures of chromium electrodeposits remained unchanged when recrystallized.

The results could be explained using the strain energy release maximization model.

Acknowledgement

This work has been supported by National Research Laboratory for texture control, Seoul National University.

References

1. G.I. FINCH, H. WILMAN and L. YANG, *Disc. Faraday Soc.* **1** (1947) 144.
2. N. A. PANGAROV, *Electrochim. Acta* **7** (1962) 139.
3. *Idem., ibid.* **9** (1962) 721.
4. D. N. LEE and Y. W. CHANG, *J. Korean Inst. Met.* **12** (1974) 243.
5. J-R. PARK and D. N. LEE, *ibid.* **14** (1976) 359.
6. G. C. YE and D. N. LEE, *Plat. and Surf. Fin.* **68** (1981) 60.
7. *Idem.*, in "Chemical Metallurgy-Attribute to Carl Wagner," edited by N. A. Gokcen (TMS-AIME, 1981) p. 493.
8. D. N. LEE, in "Proc. 3rd Asian-Metal Finishing Forum," edited by D. N. Lee (Korean Inst. Surface Eng., Seoul, 1989) p. 203.
9. *Idem.*, in "Mat. Res. Soc. Symp. Proc. Vol. 427," edited by K. N. Tu, J. W. Mayer, J. M. Poate and L. J. Chen (MRS, 1996) p. 167.
10. D. N. LEE and G. C. YE, *Plat. and Surf. Fin.* **68** (1981) 46.
11. X. YE, M. DE BONTE, J. P. CELIS and J. R. ROOS, *J. Electrochem Soc.* 139 (1992) 1592.
12. S. KANG, J. YANG and D. N. LEE, *Plat. and Surf. Fin.* **82** (1995) 67.
13. D. N. LEE, S. KANG and J. YANG, *ibid.* **82** (1995) 76.
14. J. YANG and D. N. LEE, *Met. Mater.* **5** (1999) 465.
15. H.-S. NAM and D. N. LEE, *J. Electrochem. Soc.* **146** (1999) 33.
16. D. N. LEE, *Scripta Metall. Mater.* **32** (1995) 1689.
17. A. P. SUTTON and R. W. BALLUFI, "Interfaces in Crystalline Materials" (Clarendon Press, Oxford, 1996) p. 115.
18. D. N. LEE, *Metals and Materials* **2** (1996) 121.
19. *Idem., Texture. Microstructure.* **26/27** (1996) 361.
20. S.-H. HONG, H.-T. JEONG, C.-H. CHOI and D. N. LEE, *Mater. Sci. Eng.* **A229** (1997) 174.
21. C.-H. CHOI and D. N. LEE, *Metall. Mater. Trans.* **28A** (1997) 2217.
22. D. N. LEE and H.-T. JEONG, *Scripta Metall. Mater.* **38** (1998) 1219.

23. Y. B. PARK, D. N. LEE and G. GOTTSTEIN, *Acta Mater*. **46** (1998) 3371.
24. S. H. LEE and D. N. LEE, *Mater. Sci. Eng.* **A249** (1998) 84.
25. D. N. LEE, H.-T. JEONG and H.-J. SHIN, *Met. Mater*. **4** (1998) 391.
26. D. N. LEE and H.-T. JEONG, *Mater. Sci. Eng*. **A269** (1999) 49.
27. D. N. LEE and K.-H. HUR, *Scripta Mater*. **40** (1999) 1333.
28. H. J. BUNGE, "Texture Analysis in Materials Science" (Butterworths, London, 1982).
29. C. N. REID, "Deformation Geometry for Materials Scientists" (Pergamon Press, Oxford, 1973).
30. W. C. OVERTON JR. and J. GAFFNEY, *Phys. Rev*. **98** (1997) 969.
31. D. I. BOLEF and J. DE KLERK, *ibid*. **129** (1963) 1063.

Received 12 August 1999
and accepted 14 February 2000